Zhou *et al*. *Energy Mater*. **2025**, *5*, 500077
DOI: 10.20517/energymater.2024.200

Energy Materials

Article

Open Access

Thermal degradation of lithium-ion battery cathodes: a machine learning prediction of stability and safety

Yuxin Zhou, Yifei Ding, Yuying Chen, Yinlin Shen, Zilong Wang, Xiangrong Li, Jijian Xu, Xinyan Huang*

Department of Building Environment and Energy Engineering, The Hong Kong Polytechnic University, Kowloon 999077 Hong Kong.
Department of Chemistry, City University of Hong Kong, Kowloon 999077 Hong Kong.

***Correspondence to:** Dr. Xinyan Huang, Department of Building Environment and Energy Engineering, The Hong Kong Polytechnic University, Kowloon, Hong Kong 999077, China. E-mail: xy.huang@polyu.edu.hk; ORCID: 0000-0002-0584-8452

How to cite this article: Zhou, Y.; Ding, Y.; Chen, Y.; Shen, Y.; Wang, Z.; Li, X.; Xu, J.; Huang, X. Thermal degradation of lithium-ion battery cathodes: a machine learning prediction of stability and safety. *Energy Mater.* **2025**, *5*, 500077. http://dx.doi.org/10.20517/energymater.2024.200

Received: 30 Sep 2024 **First Decision:** 13 Nov 2024 **Revised:** 12 Dec 2024 **Accepted:** 21 Dec 2024 **Published:** 27 Mar 2025

Academic Editor: Wei Tang **Copy Editor:** Fangling Lan **Production Editor:** Fangling Lan

Abstract

Lithium-ion batteries are extensively utilized due to their diverse applications, but their potential risk of thermal runaway leading to fire or even explosion remains a significant challenge to their sustainable development. The simulation of battery thermal runaway is complex, as it involves multiple reaction mechanisms. This study focuses on the interfacial interactions between reducing gases and cathode materials and explores the factors that influence these interactions during gas crosstalk within the battery. Thermogravimetric analysis coupled with differential scanning calorimetry was used to simulate the thermal attack of argon and hydrogen (H_2/Ar) mixtures on battery cathode materials to evaluate the chemical impact on the thermal runaway process. Four key material and environmental parameters, (1) cathode atomic composition; (2) hydrogen gas concentration; (3) gas flow rate; and (4) heating rate, were controlled and paired with thermal analysis curves to compile a database of 55 possible cases. Using seven input variables, this database was trained by an artificial neural network model to predict 11 critical degradation temperatures and rates for assessing material stability and safety. With an overall prediction accuracy above 0.73 (test set), we adopted an analytic hierarchy process to establish a novel scoring mechanism for cathode thermal stability. This work provides valuable insights into battery thermal runaway mechanisms and practical guidance for optimizing battery cathode chemistry.

Keywords: Li-ion battery, reductive attack, thermal stability, artificial neural network, risk assessment

INTRODUCTION

Climate change and the global energy transition drive the emerging "green and carbon-neutral" technology development towards a sustainable future. Since the early 1990s, rechargeable batteries have become integral to numerous sectors, driven by technological advancements and growing consumer demand. Among these, lithium-ion batteries (LIBs) stand out due to their high energy density, extended lifespan, eco-friendliness, and renewability. These attributes position LIBs as one of the most promising solutions for energy storage today and are widely used in people's lives[1–3]. As shown in Figure 1, a typical LIB is made of cathode, anode, electrolyte, separator, binders, and current collectors. Li-ions flow repeatedly between the anode and cathode under charging and discharging. This way, chemical energy is stored in and released from the battery, while creating an electric current.

However, once exposed to external thermal, electrical, or mechanical impacts, battery internal materials will experience considerable structural alterations[4,5]. These changes trigger a series of complex chemical reactions inside the battery, which are accompanied by the release of large amounts of heat[6]. This excessive heat can lead to thermal runaway, potentially causing large-scale fires or even explosions[7–9]. The thermal runaway process of LIBs begins with the decomposition and regeneration of the solid electrolyte interphase (SEI), and then goes through multiple physicochemical stages, such as the reaction between the electrolyte solvent and the lithium intercalated graphite (LiC_6) to generate hydrogen, the shrinkage and collapse of the separator, the decomposition of the cathode material, and the burning of electrolyte[10,11].

The LIB cathode material not only defines the electrochemical performance of the battery by its material composition, but its thermal stability also affects thermal safety and performance of the battery. Ternary nickel cobalt manganese (NCM) cathode materials primarily comprise transition metal (TM) oxides, which contribute to their superior energy density and widespread applications. However, these materials also carry a heightened risk of thermal runaway when exposed to elevated temperatures. NCMs undergo significant phase transitions, beginning with the original layered phase characterized by a $R\bar{3}m$ space group. As temperatures rise, the structure transitions to the spinel phase with a $Fd\bar{3}m$ space group and ultimately transforms into the rock-salt phase with a $Fm\bar{3}m$ space group[12]. During these phase transitions, oxygen is released due to the dominance of partially charged oxygen species within the NCM lattice[13]. When the temperature rises sufficiently, some of this oxygen escapes from the lattice and transforms into physically adsorbed molecular oxygen[14]. Ultimately, these phase transitions and the associated oxygen release contribute to the thermal instability of the battery.

This oxygen release, along with the hydrogen generated from LiH decomposition at the anode solid-electrolyte interphase above 200 °C, is generally considered to be gas crosstalk[15–17]. Some studies suggested that stabilizing the cathode crystals or capturing the released oxygen could slightly delay the onset of thermal runaway, but these methods are insufficient to prevent it entirely[18,19]. By combining thermal and gas analysis, the interfacial interaction between reducing gases and cathode materials can be revealed[20]. A reductive attack begins below 80 °C, disrupting the chemical interactions between the cathode, anode, and electrolyte. Low bond dissociation energy gases from the anode-electrolyte interface drive this attack, leading to phase transitions, oxygen release, and heat generation in the cathode. This accelerates thermal failure and triggers thermal runaway[21]. Based on this result, the safety characteristics of the thermal runaway process in LIBs can be indirectly assessed by evaluating the impact of reductive gases on the thermal stability of the cathode material. A simultaneous thermogravimetric analysis-differential scanning calorimetry (TGA-DSC) can quantify the rates of decomposition and heat release *vs*. temperature. This helps determine critical degradation temperatures and rates along with reaction heat in different thermal-runaway stages, so the thermal stability and reaction process of cathode materials under reductive gases can be evaluated. However, the data generated from TGA-DSC can be complex, making it challenging to identify meaningful patterns and relationships.

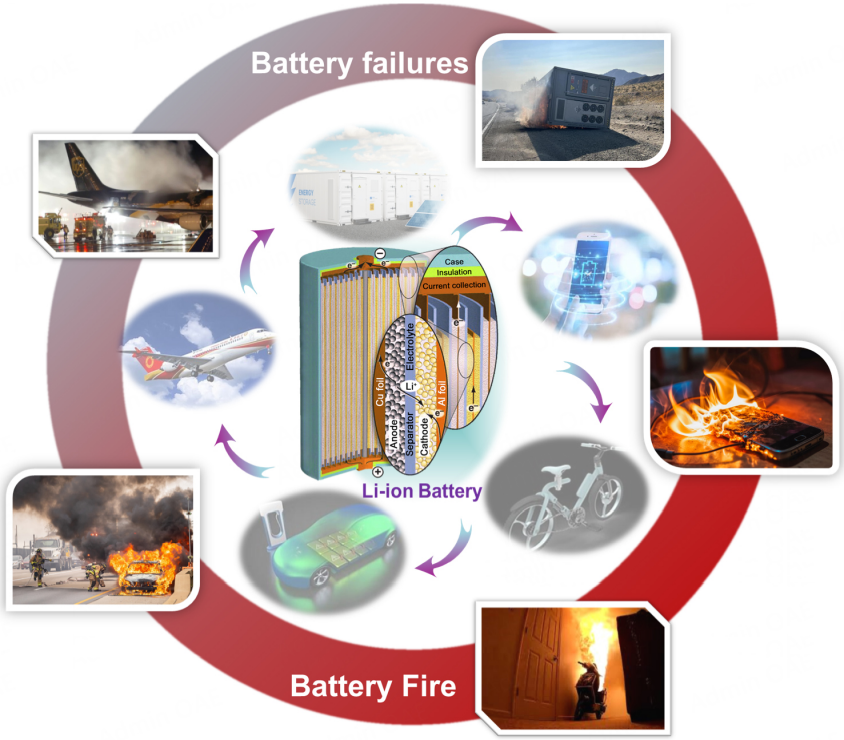

Figure 1. Panoramic view of LIB structure, applications, and failure-induced thermal runaway, fire and explosion.

The latest machine learning methods [22] show excellent performance at capturing nonlinear relationships and handling high-dimensional data, so they can make effective predictions even with incomplete information. Their powerful modeling capabilities have made machine learning a valuable tool across various fields, including battery material analysis and safety evaluation [23]. Using data from battery current, voltage, electrochemical impedance spectra, and temperature, researchers predicted parameters such as states of charge (SOCs) and battery health in the battery management system (BMS) [24]. Moreover, Artificial Neural Network (ANN) delivers highly precise predictions when applied to complex material behaviors and dynamic reactions [25–27]. The machine learning model provides valuable insights into the influence of factors such as anode and cathode structures, elemental doping, and electrolyte selection on battery performance. This understanding can guide researchers in optimizing material design [28]. Similarly, in the context of TGA, several parameters, such as temperature, heating rate, and heat flow, play crucial roles. The multilayer network structure effectively identifies complex nonlinear features and reveals intricate interactions between the variables. This capability demonstrates significant advantages in TGA data prediction [29].

Many studies have analyzed the thermophysical parameters and heat changes of overall reactions involving cathode materials, anode materials, and electrolytes [30,31]. However, a critical gap remains in linking specific reaction mechanisms to battery thermal failure or runaway, particularly regarding the effects of reducing gases on cathode materials. This study addresses this gap by examining the impact of reducing gases on ternary NCM cathode materials using TGA-DSC to investigate the reaction process and extract key thermal stability parameters. The resulting dataset was used to train an artificial neural network (ANN) model, enabling the prediction and evaluation of cathode thermal stability under varying material characteristics and environmental conditions.

Additionally, a hierarchical analysis method was applied to systematically weigh these key parameters, creating a comprehensive approach for assessing thermal stability. The findings of this research offer valuable insights

Table 1. Cathode type and composition

Cathode sample (acronym)	Mass fraction (wt.%)			
	Li	Ni	Co	Mn
$LiNi_{0.8}Co_{0.1}Mn_{0.1}O_2$ (NCM 811)	7.39	47.28	5.91	5.91
$LiNi_{0.6}Co_{0.2}Mn_{0.2}O_2$ (NCM 622)	19.75	60.29	19.76	7.32
$LiNi_{0.5}Co_{0.2}Mn_{0.3}O_2$ (NCM 523)	7.6	29.48	11.78	17.69
$LiNi_{0.33}Co_{0.33}Mn_{0.33}O_2$ (NCM 111)	7.63	20	20	18
$LiNi_{0.95}Al_{0.05}O_2$ (NCA)	7.0	53.1	5.94	0.912
$LiCoO_2$ (LCO)	7.4	-	59.7	-
$LiMn_2O_4$ (LMO)	4.21	-	-	58.86

for optimizing cathode material design to enhance safety, developing effective thermal management strategies for battery systems, and informing material selection in commercial battery manufacturing. By deepening the understanding of cathode stability and providing predictive tools for novel materials, this study addresses critical safety challenges in LIB technology, supporting the development of safer and more reliable next-generation energy storage solutions.

EXPERIMENTS AND METHODOLOGIES

Preparation of material

A range of cathode materials purchased from Cardo without further treatment were used to compare the performance of various elemental compositions after being attacked by reducing gases. The compositions of these cathodes are shown in Table 1. CR2032-type coin cells were assembled in an argon-filled glove box to investigate the thermal stability of cathode materials in LIBs with different SOCs under a hydrogen atmosphere. For the fabrication of electrodes, a viscous slurry containing purchased NCM cathode materials, Super P, and polyvinylidene fluoride (PVDF) in a mass ratio of 70:20:10 was prepared. The slurry was cast onto an aluminum foil and dried overnight at 100 °C under vacuum. For CR2032 cells, lithium foil served as both the reference and counter electrodes, while the electrolyte used was a 1.0 M solution of $LiPF_6$ in a 1:1 (v/v) mixture of ethyl carbonate and diethyl carbonate (EC/DEC). Celgard 2325 25 μm trilayer microporous membrane [polypropylene/polyethylene/polypropylene (PP/PE/PP)] was used as the separator.

The charge and discharge tests were performed using a Neware battery measurement system in a voltage range of 2.75-4.2 V (*vs*. Li^+/Li) at 0.1 C. For the cell at the charge state of 100% (SOC-100), it was charged with a constant current of 0.1 C from the open circuit potential (OCP) to the cut-off voltage of 4.2 V and then with a constant voltage until the charging current decreased to 0.02 C. The practical specific capacity was controlled to obtain the cells with other SOCs. The charge and discharge curves of NCM811 were shown as examples in Supplementary Figure 1. In the preparation of the samples for characterization, the electrode materials were disassembled from cells, washed three times using Dimethoxyethane (DME) and N-Methylpyrrolidone (NMP), and then dried at 60 °C for 12 h under vacuum.

Thermal analysis setup

Simultaneous thermal analysis (TGA-DSC) was conducted using a PerkinElmer STA6000 under three different hydrogen gas contents of a hydrogen and argon mixture: 5%, 3%, and 1% H_2. The gas flow rates were set at 50, 100, and 150 mL/min. Before the test, all materials and crucibles were dried in an oven at 80 °C for 12 h to ensure that the experiment would not be affected by moisture. In this study, non-isothermal heating was applied, where 5-7 mg of sample was heated from room temperature to 800 °C at three rates of 10, 30, and 60 °C/min. Each test was repeated at least twice to ensure good experimental reproducibility, with a relative error of ±2% under the same conditions. Each ternary material has the same experimental setup and all the experimental scenarios are shown in Table 2.

Table 2. TGA experimental scenarios

Number	SOC (%)	H_2 vol. fraction (%)	Heating rate (K/min)	Gas flow rate (mL/min)
1	0	5	10	100
2	0	3	10	100
3	0	1	10	100
4	0	5	10	50
5	0	5	10	150
6	0	5	30	100
7	0	5	60	100
8	50	5	10	100
9	50	1	10	100
10	100	5	10	100
11	100	1	10	100

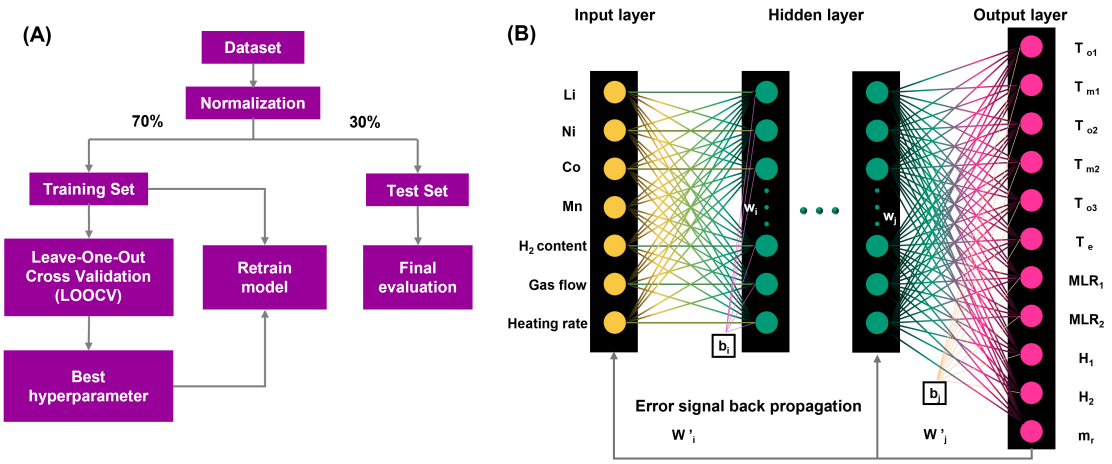

Figure 2. (A) Training flow of the TG data prediction model and (B) architecture of the developed ANN model.

Table 3. The AHP model for cathode thermal risk under hydrogen attack

Target	Category	Parameter	Weight	Specifications
Cathode thermal risk under hydrogen attack (R)	Critical degradation temperature (T)	T1	0.2873	Onset temperature of decomposition reaction T_{o1}
		T2	0.1427	Onset temperature of reduction reaction T_{o2}
		T3	0.0894	Onset temperature of structural collapse T_{o3}
		T4	0.0503	Temperature at peak decomposition rate T_{m1}
		T5	0.0319	Temperature at peak reduction reaction rate T_{m2}
		T6	0.0216	End temperature of reaction T_e
	Reaction mass loss (M)	M1	0.0225	Peak decomposition rate MLR_1
		M2	0.074	Peak reduction rate MLR_2
		M3	0.0408	Mass remaining m_r
	Heat release of reaction (H)	H1	0.2053	Heat Release during decomposition H_1
		H2	0.0342	Heat absorption during reduction H_2

Machine learning methods

The ANN model, a commonly used machine learning method for supervised learning tasks, consists of an input layer, hidden layers, and an output layer. In this study, static timing analysis (STA) data is analyzed using the back-propagation (BP) algorithm within an ANN framework, as shown in Figure 2A. The BP algorithm, which iteratively minimizes the error between predicted and actual outputs by adjusting the network's weights, ensures an effective learning process and reliable prediction results. Key information was extracted from the TGA data to establish a database. The input layer consists of seven input variables, namely content of Li, Co, Ni, and Mn; H_2 content; gas flow rate and heating rate. Meanwhile, 11 output variables are linked: T_{o1}, T_{m1}, T_{o2}, T_{m2}, T_{o3}, T_e, MLR_1, MLR_2, H_1, H_2 and m_r, which are explained in Table 3 and Figure 2B.

For each neuron depicted in Figure 2B, the output is determined by

$$Out_j = h\left(\sum_{i=1}^{N} W_{ji}X_i + B_j\right) \quad (1)$$

where X_i represents the input from the neuron in the previous layer, W_{ji} denotes the weight associated with X_i, B_j is the bias, and h signifies the activation function. The activation functions selected for this study included the rectified linear unit (ReLU), the hyperbolic tangent (tanh), and logistic functions, which introduce non-linearity into the model, enhancing its ability to capture intricate patterns. The sigmoid function was utilized as the activation function between each layer.

In this study, an ANN model with five hidden layers was developed using the Scikit-Learn library in Python to predict the thermal properties of cathode materials. Firstly, the whole dataset is normalized to improve the convergence speed of the ANN during training. Then the dataset is divided into 70% for training and 30% for testing in order to evaluate the model's prediction accuracy and robustness. Because of the limited dataset size, the leave-one-out cross-validation (LOOCV) technique is utilized for both model selection and parameter optimization. In this technique, each observation in the training set is used once as a validation sample while the remaining samples are used for training. This procedure is repeated for each observation, and the average performance metric is computed. The final model will select the best-performing hyperparameters based on the evaluation performance metrics.

Performance evaluation

The performance of the developed ANN model is evaluated by comparing the predicted values to the actual experimental data. This comparison is quantified using several well-known evaluation metrics.

One commonly used metric is the mean squared error (MSE), which is defined as

$$MSE = \frac{1}{N}\sum_{i=1}^{N}\left(Y_{pred} - Y_{actu}\right)^2 \quad (2)$$

Another important metric is the coefficient of determination (R^2), which is defined as

$$R^2 = 1 - \frac{\sum_{I=1}^{N}\left(Y_{pred} - Y_{actu}\right)^2}{\sum_{I=1}^{N}\left(Y_{pred} - Y_{mean}\right)^2} \quad (3)$$

where Y_{pred} represents the predicted value, while Y_{actu} stands for the actual value. N denotes the number of datasets.

The MSE measures the average of the squared errors between predicted and actual values, providing an indication of the model's prediction accuracy. The R^2 metric measures how well the independent variables explain the variability in the dependent variable. A higher R^2 value suggests that the model captures more of the variance in the data, reflecting a better fit.

AHP quantitative scoring method

The hierarchical analysis method is employed to establish a risk assessment framework for the hydrogen attack reaction. During the reaction process of hydrogen attack on the cathode, key parameters are classified into secondary indicators, which are further grouped into three primary evaluation indicators: critical degradation temperature of cathode reaction (T), reaction mass loss (M), and heat release of reaction (H). T was divided into six sub-factors (T1-T6), M into three sub-factors (M1-M3), and H into two sub-factors (H1, H2). These primary indicators collectively assess the risk of thermal runaway in the cathode under H_2 exposure. The weight of each index in the evaluation system signifies the significance of each factor. By assigning scores to

different factor layers, a judgment matrix is formed to determine their relative weights. The importance scale between the two factors is provided in Supplementary Table 1. Based on the process of hydrogen attack on the cathode, the factors are ranked as follows: T > H > M. The relative importance obtained from comparisons between each group is processed accordingly; the judgment matrix R is as follows:

$$R = \begin{bmatrix} a_{11} & \cdots & a_{in} \\ \vdots & \ddots & \vdots \\ a_{n1} & \cdots & a_{nn} \end{bmatrix} \tag{4}$$

Here, a_{ij} represents the importance ratio of factor i to factor j, and n denotes the number of index factors at each level. R is a reciprocal matrix where a_{ij} and a_{ji} are reciprocals.

The normalization of R' s columns is given below:

$$\overline{a_{ij}} = \frac{a_{jj}}{\sum_{k=1}^{n} a_{kj}} (i, j = 1, 2, 3, \cdots, n) \tag{5}$$

Calculate the sum of the elements in each row:

$$\overline{w_{ij}} = \frac{n}{\sum_{i=1}^{n} \overline{a_{ij}} (i, j = 1, 2, 3, \cdots, n)} \tag{6}$$

Re-normalize to obtain the weight of each factor at this level:

$$w_i = \frac{\overline{w_i}}{\sum_{i=1}^{n} \bar{w}_l} (i, j = 1, 2, 3, \cdots, n) \tag{7}$$

The weight of each evaluation factor in the lowest layer of the evaluation system is derived as follows:

$$C_{ijk} = C_i C_j C_k \tag{8}$$

The cathode thermal property judgment matrix can be established [Supplementary Tables 2-5]. The random consensus index RI shown in Supplementary Table 6 is used to evaluate the consistency of the judgment matrix. A secondary evaluation model was developed, as shown in Table 3.

RESULTS AND DISCUSSION

Hydrogen attack cathode performance

The properties of NCM cathode materials that have not undergone delithiation remain highly stable. As shown in Figure 3A, the mass loss of NCM811 powder exhibits minimal change when heated in an inert Ar atmosphere from 30-800 °C. A slight mass loss is only observed once the temperature exceeds 695 °C. By the end of the experiment at 800 °C, the total mass loss is still just 1.5%. This phenomenon is likely a result of slight phase transitions occurring within the cathode material lattice at elevated temperatures, leading to the release of a limited quantity of oxygen gas[13]. The effect of hydrogen on NCM cathodes can be revealed by introducing varying concentrations of H2 (balanced with Ar) as the reductive gas. The results, presented in Figure 3B-D,

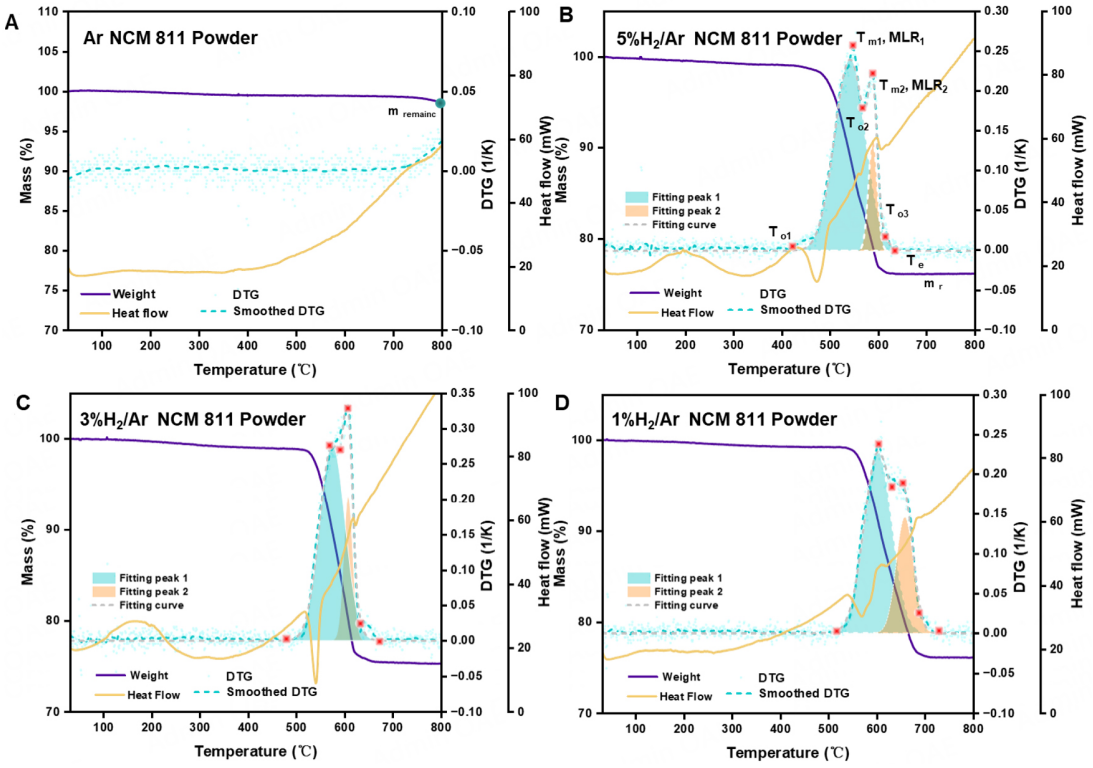

Figure 3. Non-isothermal decomposition behavior of cathode in various atmospheres (A) Ar, (B) 5%H_2/Ar, (C) 3% H_2/Ar, (D) 1% H_2/Ar.

demonstrate significant changes in the thermal decomposition behavior of NCM. The onset of decomposition reactions starts at lower temperatures (400-500 °C), accompanied by significant mass loss.

The comparison of Figure 3B-D shows that the cathode curves in the H_2/Ar atmosphere exhibit similar characteristics. The cathode decomposition is consistently dominated by two reactions, resulting in a rapid mass loss. Additionally, a brief period of rapid mass loss occurs before the cathode mass stabilizes. With the onset of cathode decomposition in Ar taking place above 695 °C, the earlier decomposition observed in the H_2/Ar atmosphere is attributed primarily to the interaction between H_2 and the cathode, that is, the reducing attack. As the temperature rises, H_2 accelerates the cathode decomposition, causing greater structural damage. H_2 penetrates deeper into the particle core, promoting the transformation of the layered structure into spinel and rock-salt phases. This transformation leads to an increased release of oxygen, which may result in greater mass loss. The three TMs in ternary cathode materials each contribute differently to the material's structure and properties.

Typically, the redox pairs $Ni^{2+/3+}$ and/or $Ni^{3+/4+}$ are responsible for most of the reversible capacity. Cobalt, through its $Co^{3+/4+}$ redox reactions, improves the layered arrangement of the structure. Additionally, manganese helps stabilize part of the structure due to the electrochemical inertness of Mn^{4+}. In other words, the impact on the ionic chemical stability in the layered structure decreases in the following order: Co > Ni > Mn. As a result, $Ni^{3+/4+}$ and $Co^{3+/4+}$ in NCM may be reduced to $Ni^{2+/3+}$ and $Co^{2+/3+}$, forming NiO, Ni_2O_3, Co_3O_4 and CoO, while Mn remains in the form of $LiMnO_2$ [32,33]. The possible chemical reactions involved for ionic decomposition include

$$\begin{gathered} LiNi_xCo_yMn_zO_2\ (\text{layer}) \rightarrow \\ iLi_2O + xNiO(\text{rock-salt}) + yLiCoO_2(\text{spinel}) + zLiMnO_2(\text{spinel}) + O_2(g) \end{gathered} \tag{9}$$

$$3LiCoO_2\ (spinel)\ \rightarrow 1.5Li_2O + Co_3O_4\ (rock\text{-}salt)\ + 0.25O_2(\ g) \tag{10}$$

$$LiCoO_2\ (spinel)\ \rightarrow 0.5Li_2O + CoO\ (rock\text{-}salt)\ + 0.25O_2(\ g) \tag{11}$$

$$H_2 + 0.5O_2 \rightarrow H_2O \tag{12}$$

As hydrogen continues to flow and the temperature increases, the cathode decomposes into a rock-salt phase. Hydrogen then further reduces the cathode to metal. This is reflected by the endothermic peaks in Figure 3. The possible reactions involved in hydrogen attack[34–36] include

$$NiO + H_2 \rightarrow Ni + H_2O \tag{13}$$

$$Co_3O_4 + 4H_2 \rightarrow 3Co + 4H_2O \tag{14}$$

$$CoO + H_2 \rightarrow Co + H_2O \tag{15}$$

The weak differential thermogravimetry (DTG) peaks observed before the cathode mass stabilizes can be attributed to the structural collapse of $LiMnO_2$ according to:

$$2LiMnO_2(\ spinel\ ) \rightarrow Mn_2O_3(rock\text{-}salt) + Li_2O \tag{16}$$

This is due to the electrochemical inertness of Mn and its low content in NCM. As the experiments did not include crystalline phase analysis or elemental composition characterization of the reaction products, the formulas only suggest the possible presence of these products without precisely determining their content.

To more accurately characterize the cathode decomposition process, key parameters were extracted based on the specific features of the curves, including T_{o1}, T_{m1}, T_{o2}, T_{m2}, T_{o3}, T_e, MLR_1, MLR_2, H_1, H_2 and m_r. In detail, T_{o1} represents the initial decomposition temperature of the cathode, marking the onset of the decomposition reaction when the DTG value exceeds 0.001. MLR_1 and T_{m1} refer to the maximum decomposition rate and the corresponding temperature during the cathode phase transition and decomposition. The heat released during this process is denoted by H_1. T_{o2} indicates the starting temperature of the reduction reaction for rock-salt phase metal oxides. MLR_2 and T_{m2} represent the peak reduction rate and the corresponding temperature, with the associated heat absorption marked as H_2. T_{o3} is related to the collapse of $LiMnO_2$. T_e specifies the end temperature of the entire reaction process where H_2 interacts with the cathode, and m_r refers to the percentage of cathode mass remaining.

Table 4 presents the key reaction parameters of the cathode at varying H_2 contents. In 1% H_2/Ar, the onset decomposition temperature of NCM811cathode is 513 °C, which is 182 °C lower than in pure Ar. As the hydrogen content increases, the onset temperature shifts lower, with decomposition starting at 439 °C in 5%

Table 4. Key parameters of NCM 811 in various atmospheres, where the negative heat of reaction means an exothermic process

Reduction gas	T_{o1} °C	T_{m1} °C	T_{o2} °C	T_{m2} °C	T_{o3} °C	T_e °C	MLR_1 (1/K)	MLR_2 (1/K)	m_r (%)	H_1 (J/g)	H_2 (J/g)
5%H_2/Ar	439	547	568	587	615	623	0.25	0.22	76.1	-510	161
3%H_2/Ar	497	574	586	607	624	660	0.22	0.33	75.3	-452	59
1%H_2/Ar	513	603	625	657	695	707	0.19	0.24	76.1	-335	37

Table 5. Key parameters of various cathodes in 5%H_2/Ar

Cathode material	T_{o1} °C	T_{m1} °C	T_{o2} °C	T_{m2} °C	T_{o3} °C	T_e °C	MLR_1 (1/K)	MLR_2 (1/K)	m_r (%)	H_1 (J/g)	H_2 (J/g)
NCM811	439	547	568	587	615	623	0.25	0.22	76.09	-510	161
NCM622	524	587	595	610	633	659	0.31	0.34	77.56	-465	178
NCM523	555	613	619	627	650	678	0.38	0.40	76.75	-261	241
NCM111	551	606	621	627	650	680	0.40	0.33	74.84	-179	152

H_2. Similarly, T_{m1}, T_{o2}, T_{m2}, T_{o3}, and T_e, also occur earlier as T_{o1} advances. The increase in MLR_1 with higher hydrogen contents may be due to the greater structural damage inflicted on the cathode by more H_2. At 5%H_2/Ar, the cathode decomposition releases 540 J/g of heat, which is also positively correlated with the H_2 content. The weaker correlation between MLR_2 and hydrogen content might result from the random distribution of cracks on the cathode particle surface. Additionally, the O_2 released from the reduction of rock-salt phase metal oxides may not fully escape from the particles. At higher H_2 content, the formation of rock-salt phase metal oxides increases, leading to greater heat absorption H_2 in subsequent reduction reactions.

Figure 4 and Table 5 illustrate the non-isothermal decomposition behavior of various cathodes in 5%H_2/Ar curves and data. The decomposition processes of NCM622, NCM523, and NCM111 cathode materials are similar to that of NCM811. The decomposition temperatures for NCM622, NCM523, and NCM111cathode materials are 524, 555, and 551 °C, respectively, lagging that of NCM811 by 85, 116, and 112 °C, which indicates a negative correlation between thermal stability and Ni content in the cathode. In this study, a non-isothermal heating mode is employed, where reaction time and temperature are linearly related. Thus, greater temperature differences correspond to longer reaction times. The differences in onset temperature and maximum decomposition rate for NCM811, NCM622, NCM523, and NCM111 cathode materials are 108, 63, 58, and 55 °C, respectively.

This trend suggests a diminishing gap in both temperature and time, resulting in a reduction of oxygen release. This reduction is attributed to the instability of high-valence TM ions under hydrogen attack and elevated temperatures. Such instability leads to the reduction of these ions and the release of oxygen from the lattice to maintain charge neutrality. Notably, Ni ions exhibit the fastest reduction rate, indicating their significant influence on the thermal stability of the cathode [37,38]. For a fixed lithium content, oxygen in the local coordination structure becomes less stable with increased Ni, particularly in higher oxidation states.

Consequently, materials with higher Ni content exhibit lower thermal decomposition temperatures and greater oxygen release. The differences between T_{m2} and T_{o2} for the four types of cathodes are 19, 15, 8, and 6 °C, respectively. This indicates that a decrease in Ni content reduces the amount of reducible rock-salt metal oxides. Consequently, this leads to a more rapid end of the reduction reaction. The mass loss peaks for Mn become more distinct with increasing Mn content in the cathode. The Mn mass loss peaks are 0.058, 0.090, and 0.081 for NCM622, NCM523, and NCM111, respectively, suggesting the enhanced reduction of Mn by H_2. The TGA results in Supplementary Figure 2 for the corresponding oxides of $LiNi_{0.95}Al_{0.05}O_2$ (NCA), $LiCoO_2$ (LCO) and $LiMn_2O_4$ (LMO) further support this observation. Under hydrogen attack, NCA shows mass loss at temperatures below 400 °C, whereas LMO remains the stable structure till about 700 °C.

In addition to the analysis of the cathode composition, the decomposition reactions influenced by environ-

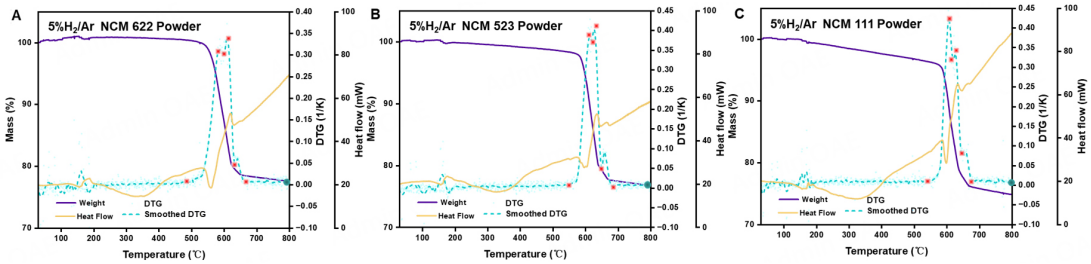

Figure 4. Non-isothermal decomposition behavior of various cathodes in 5%H_2/Ar (A) NCM 622, (B) NCM 523, (C) NCM 111.

Table 6. Key parameters of NCM 811 cathodes at various gas flow and heating rates in 5%H_2/Ar

Heating rate (°C/min)	Flow rate (mL/min)	T_{o1} °C	T_{m1} °C	T_{o2} °C	T_{m2} °C	T_{o3} °C	T_e °C	MLR_1 (1/K)	MLR_2 (1/K)	m_r (%)	H_1 (J/g)	H_2 (J/g)
10	50	519	567	576	591	633	674	0.27	0.30	78.7	-518	251
10	150	424	532	553	579	606	647	0.24	0.24	70.8	-	-
30	100	484	617	645	672	703	713	0.18	0.17	76.6	-501	136
60	100	534	684	726	749	800	800	0.14	0.12	76.3	-443	54
10	100	439	547	568	587	615	623	0.25	0.22	76.1	-510	161

mental changes are also investigated. The flow rate of 5%H_2/Ar was adjusted to 50 and 150 mL/min, while maintaining a constant heating rate of 10 °C/min. Data presented in Figure 5 and Table 6 reveal that the flow rate of H_2 affects the reaction similarly to its content. At a flow rate of 50 mL/min, the onset temperature of the decomposition reaction is 80 °C lower than at 100 mL/min. Conversely, at a flow rate of 150 mL/min, the onset temperature rises to 424 °C, which is 15 °C higher than expected. The flow of H_2/Ar not only reacts with the cathode but also provides a purging effect. At 50 mL/min, the exothermic heat released (H_1) is -518.37 J/g, likely due to reduced convective heat transfer between the material and the gas at lower flow rates. However, at 150 mL/min, the heat generated from the reaction could not be effectively captured. This can be attributed to the high flow rate, which rapidly purges the heat released from the reaction, resulting in heat loss.

The onset temperatures of the reaction were 484 and 534 °C at heating rates of 30 and 60 °C/min, respectively. This indicates that the onset temperature increases with a higher heating rate, which can be explained by reaction kinetics. According to the Arrhenius Law, the reaction rate constant K is related to the temperature T and the activation energy E_a [39], as given in

$$k = Ae^{-\frac{Ea}{RT}} \tag{17}$$

An increased heating rate may prevent the molecules in the sample from achieving the requisite reaction rate, as they may not acquire sufficient energy in time. Consequently, the decomposition reaction commences at a higher temperature. Despite the rapid rise in temperature, the molecules may still lack the necessary energy to overcome the activation barrier for decomposition. This phenomenon further elevates the onset temperature.

Conversely, maximum weight loss rates (MLR_1, MLR_2) were negatively correlated with the heating rate. At 30 °C/min, MLR_1, MLR_2 values were 0.18 and 0.17, respectively. At 60 °C/min, these values decreased to 0.14 and 0.12. This trend suggests that the rapid heating rate may inhibit complete decomposition, leading to fewer rock-salt phase products and consequently affecting the reduction rate. As a result, the exothermic heat H_1 also diminishes.

During the battery charging process, Li^+ ions are removed from the cathode layers and embedded into the anode layers. The degree of delithiation corresponds to the battery SOC. Figure 6 and Table 7 illustrate the decomposition behavior and key parameters of NCM811 at different SOCs under hydrogen attack in non-

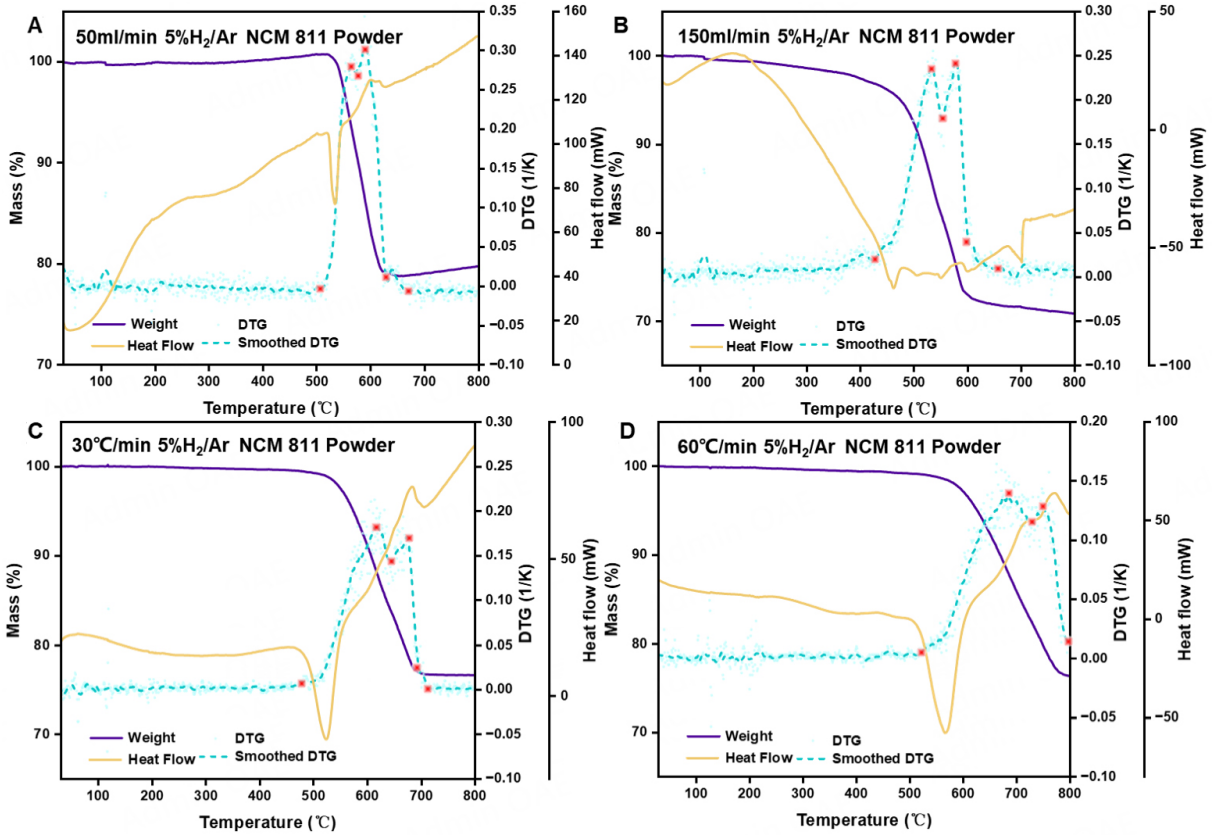

Figure 5. Non-isothermal decomposition behavior of gas flow and heating rate in 5%H_2/Ar (A) 50 mL/min,10 °C/min, (B) 150 mL/min, 10 °C/min, (C) 30 °C/min, 100 mL/min, (D) 60 °C/min, 100 mL/min.

isothermal conditions (Heating rate:10 °C/min, gas flow: 100 mL/min). Compared to a cathode that has not undergone charging or discharging, a distinct mass loss occurs before the exothermic peak of the cathode's decomposition. This relates to a localized mass loss peak in the DTG curves (marked in red in the figure). This mass loss, observed before 100 °C, may be due to side reactions involving the electrolyte during charging, such as the oxidation of electrolyte components and the degradation of $LiPF_6$. These reactions lead to the formation of a dense cathode-electrolyte interface (CEI) film on the cathode surface, covering the secondary particles so thoroughly that the original structure of the primary particles is nearly indistinguishable.

The CEI film - mainly composed of Li_2CO_3, LiF, and other compounds - forms on the cathode surface during cycling. Before hydrogen attacks the cathode, the CEI will undergo thermal decomposition, releasing gases such as CO_2 and CO, leading to an initial mass loss [40,41]. For the NCM811 cathode analyzed here, excluding the Li, Ni, Co, and Mn elements, the oxygen content is approximately 33.5 wt%. Upon complete decomposition of the cathode and the release of oxygen, the remaining mass should be greater than 66.5%. However, for the cathode at 100% SOC, the remaining mass after decomposition is 59.4%, indicating the presence of the CEI film. Once the CEI film decomposes, the cathode is directly exposed to H2. As the cathode is attacked by both hydrogen and high temperature, further decomposition occurs. The T_{o1} for the 100% SOC, 50% SOC, and 0% SOC cathodes are 162, 178, and 307 °C, respectively. Correspondingly, in H_2/Ar, the maximum weight loss rates (MLR_1) for the 100% SOC, 50% SOC, and 0% SOC cathodes are 0.31, 0.18, and 0.06, respectively. These results show that the cathode decomposes more easily with higher SOC, likely due to cation mixing and lithium vacancy formation.

Since Ni^{2+} (0.069 nm) and Li^+ (0.076 nm) have a similar ionic radius, Ni^{2+} can migrate from the TM layer to ad-

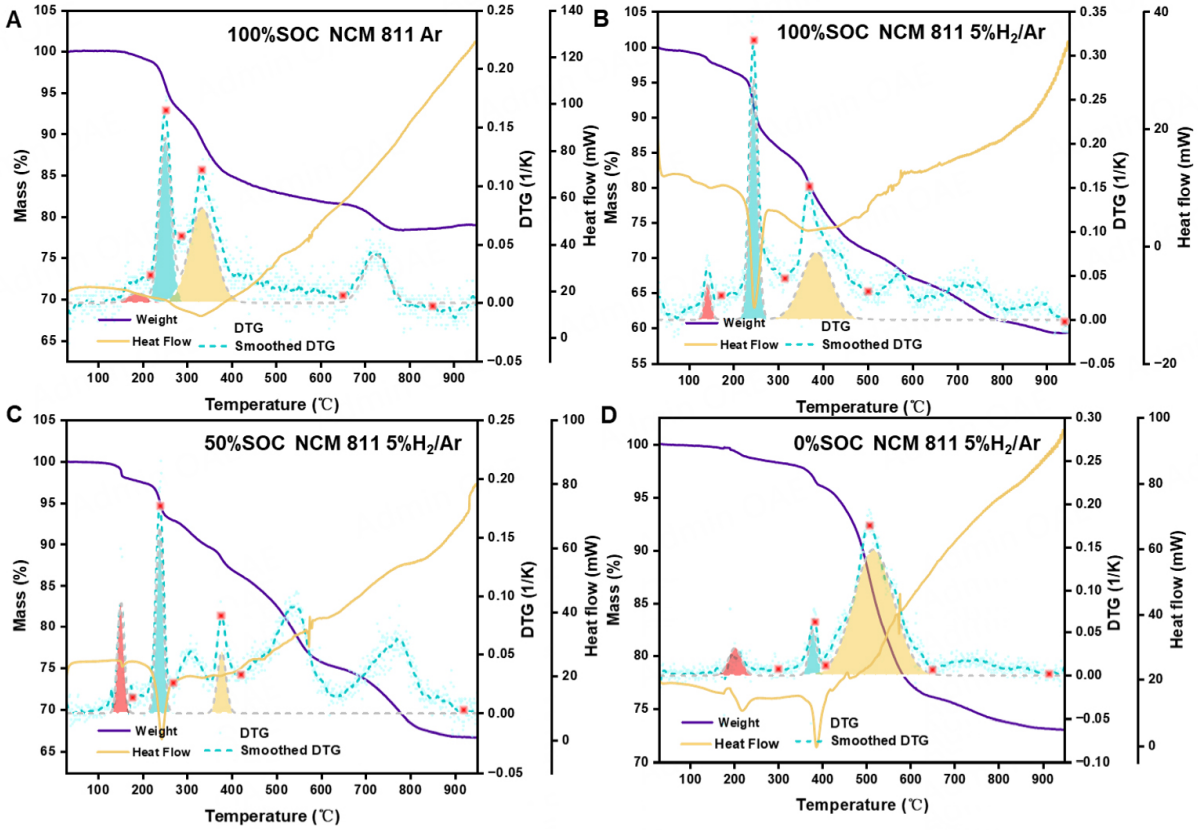

Figure 6. Non-isothermal decomposition behavior of NCM811 various SOCs (A) 0% SOC 5%H_2/Ar, (B) 50% SOC 5%H_2/Ar, (C) 100% SOC 5%H_2/Ar, (D) 100% SOC Ar.

Table 7. Key parameters of various SOC NCM 811 cathodes under 5%H_2/Ar and Ar

SOC (%)	Reduction gas	T_{o1} °C	T_{m1} °C	T_{o2} °C	T_{m2} °C	T_{o3} °C	T_e °C	MLR_1 (1/K)	MLR_2 (1/K)	m_r (%)	H_1 (J/g)
0%	5%H_2/Ar	307	380	399	509	657	915	0.06	0.18	73.1	-358.5
50%	5%H_2/Ar	178	237	271	376	415	950	0.18	0.08	66.7	-396.2
100%	5%H_2/Ar	162	239	312	377	495	950	0.31	0.31	59.4	-651.0
100%	Ar	216	248	278	332	627	854	0.16	0.11	79.0	-

jacent lithium vacancies after Li^+ detachment, leading to cation mixing. This phenomenon significantly affects the performance, structure, and thermal stability of the cathode[42]. At high SOC, the excess lithium vacancies are thermodynamically unstable, driving the cathode decomposition to restore equilibrium[43]. Moreover, hydrogen attack and elevated temperatures accelerate the decomposition process, reducing the onset temperature of charged cathodes compared to those that remain untreated. As SOC increases, the exothermic heat of the decomposition reaction also rises, indicating a higher risk of thermal runaway in batteries with higher SOC.

Analysis of Pearson correlation coefficient

The thermal decomposition behavior of hydrogen-attacked cathode materials is influenced by several factors, including cathode composition, degree of delithiation, hydrogen content, gas flow rate, and heating rate. Decomposition experiments were also conducted on NCM622, NCM523, and NCM111 under varying conditions, resulting in a dataset comprising 55 entries. To enhance the accuracy of data predictions, relevant features and variables were selected from the dataset, and Pearson correlation analysis was employed to elucidate the relationships between these parameters.

The Pearson correlation coefficient is a statistical measure that quantifies the linear relationship between two real-valued variables. Introduced as the first formal metric for correlation, it remains the most commonly applied method today. This coefficient is particularly useful for evaluating the linear association between two normally distributed continuous variables[44] and can be expressed as:

$$r = \frac{cov_{x,y}}{\sigma_x \cdot \sigma_y} = \frac{\sum (x_i - \bar{x})(y_i - \bar{y})}{\sqrt{\sum (x_i - \bar{x})^2}\sqrt{\sum (y_i - \bar{y})^2}} \tag{18}$$

where $cov_{x,y}$ represents the covariance between variables x and y, while σ_x and σ_y refer to the standard deviations of x and y, respectively. The terms $\bar{x}$ and $\bar{y}$ represent the mean values of each variable. A coefficient value approaching 1.0 signifies a strong positive correlation, whereas a value near -1.0 indicates a strong negative correlation.

Additionally, to assess whether the correlation coefficient is statistically significant, the t-score and P-value are computed for further evaluation:

$$t = \frac{r\sqrt{n-2}}{\sqrt{1-r^2}} \tag{19}$$

where n represents the sample size, with degrees of freedom equal to n-2, and r is the Pearson correlation coefficient. Subsequently, the P-value is determined as the two-sided P-value corresponding to the t-distribution with n-2 degrees of freedom. Typically, a P-value of less than 0.05 is considered statistically significant, while a value below 0.001 is regarded as highly significant by most researchers.

Figure 7 presents the half Pearson correlation coefficient (r) matrix, with each row corresponding to a variable in the dataset and each column representing the same variables as the rows. The values in each cell indicate the correlation coefficient between the two associated variables. The lithium content in the cathode exhibits strong correlations with T_{o1}, T_{m1}, T_{o2}, and T_{m2}, with coefficients of 0.79, 0.85, 0.85, and 0.78, respectively. This indicates that a lower removal of lithium from the cathode corresponds to higher initiation temperatures for decomposition, which subsequently influences the temperatures of ensuing reactions. The positive correlation between lithium content and the remaining mass also highlights that cathodes with higher SOC retain less mass at the conclusion of the reaction. Additionally, the correlation coefficient of 0.48 between lithium content and H_1 suggests that cathodes with higher Ni content face a greater risk of thermal runaway.

It is worth noting that the strong correlation may not be apparent in the correlation coefficient plot. This is likely due to the limited variation in the T_{o1} across different hydrogen contents. However, the correlation coefficient between hydrogen content and heat absorption during the reduction reaction is 0.42, while MLR_2 correlates with H_2 at 0.64. These values reinforce the earlier observation that increased hydrogen content accelerates mass loss and enhances heat absorption during the reduction process. Furthermore, the key parameters in the thermal decomposition of the cathode exhibit very high intercorrelations. Specifically, the correlation coefficients of T_{o1} with T_{m1}, T_{o2}, T_{m2}, and T_{o3} are 0.97, 0.94, 0.92, and 0.85, respectively, clearly indicating that hydrogen attack significantly influences the sequential reactions involved in cathode decomposition.

Evaluation of machine learning prediction

The experimental data and Pearson correlation analysis reveal a distinct correlation among the properties of cathode materials, experimental conditions, and key parameters during the hydrogen attack. This finding suggests the feasibility of developing a machine learning model to predict the thermal decomposition behavior

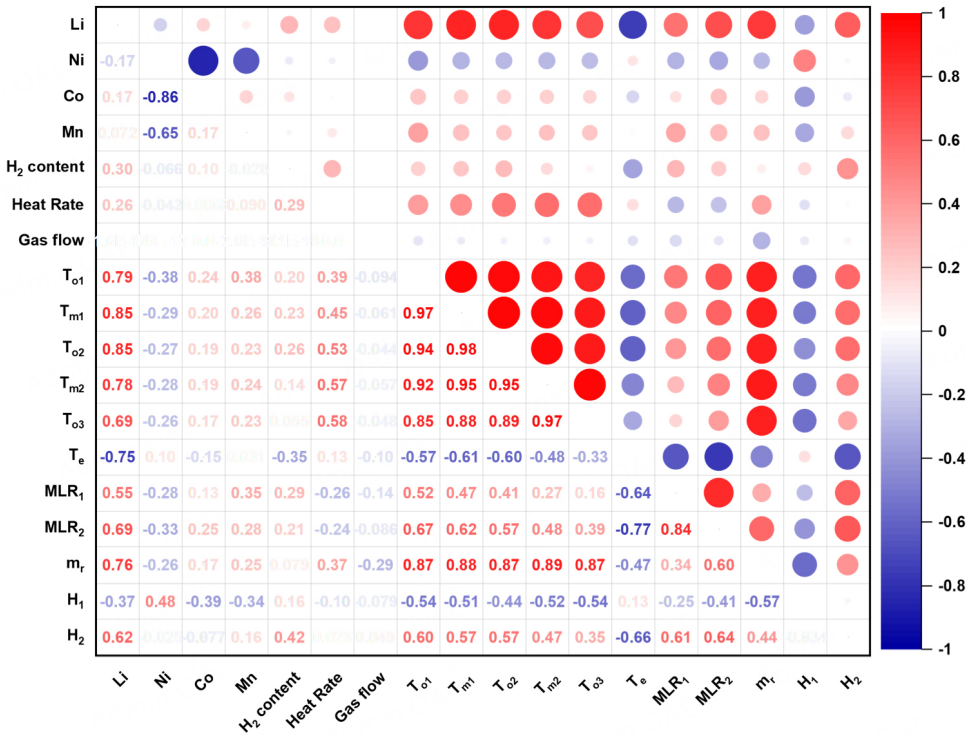

Figure 7. Pearson correlation coefficient (r) among any two variables in the dataset.

of cathode materials. By using this data-driven approach, the model can analyze and forecast crucial factors such as reaction temperature, mass loss rate, and thermal effects under various reaction conditions. The seven input variables for the model include the atomic ratios of Li, Co, Ni, and Mn, as well as H_2 content, gas flow rate, and heating rate. The model aims to predict 11 output variables: T_{o1}, T_{m1}, T_{o2}, T_{m2}, T_{o3}, T_e, MLR_1, MLR_2, H_1, H_2, and m_r.

The optimal hyperparameters for the models were identified using LOOCV and then applied to retrain the prediction model. For the ANN model, hyperparameters were determined through trial-and-error optimization on the training set. This selection reflects a careful balance to enhance model performance. The tanh activation function was chosen for its effectiveness in handling nonlinear problems, while also mitigating gradient vanishing issues to maintain model stability. A regularization coefficient (alpha) of 0.01 was used to penalize weights moderately, reducing overfitting and improving generalization. The hidden layer architecture, with neurons configured in a five-layer structure (16, 32, 64, 64, 32), was designed to capture high-dimensional data features and process complex information. An initial learning rate of 0.01 allows the model to converge quickly during early training, while also ensuring stability in later stages. With a maximum of 300 iterations, the model has sufficient opportunities to reach optimal convergence. The optimizer, stochastic gradient descent (SGD), is well-suited for large datasets and helps avoid local minima. Finally, the convergence tolerance was set to $1e^{-}06$, ensuring that training stops once high accuracy is achieved. This hyperparameter configuration strikes a balance between training efficiency and generalization, enabling the model to deliver stable performance even under complex experimental conditions.

Supplementary Figure 3 illustrates the R^2 *vs*. loss curve, revealing that the R^2 for the training set converges to 0.75, while the mean square error (MSE) approaches 0, confirming the stability of the training process and the absence of overfitting. The predicted *vs*. actual values for the test set are shown in Figure 8, demonstrating good prediction performance. The point distribution is close to the diagonal, with most data points situated in the region where the error is less than 20%, indicating accurate predictions. The R^2 for the test set is 0.73,

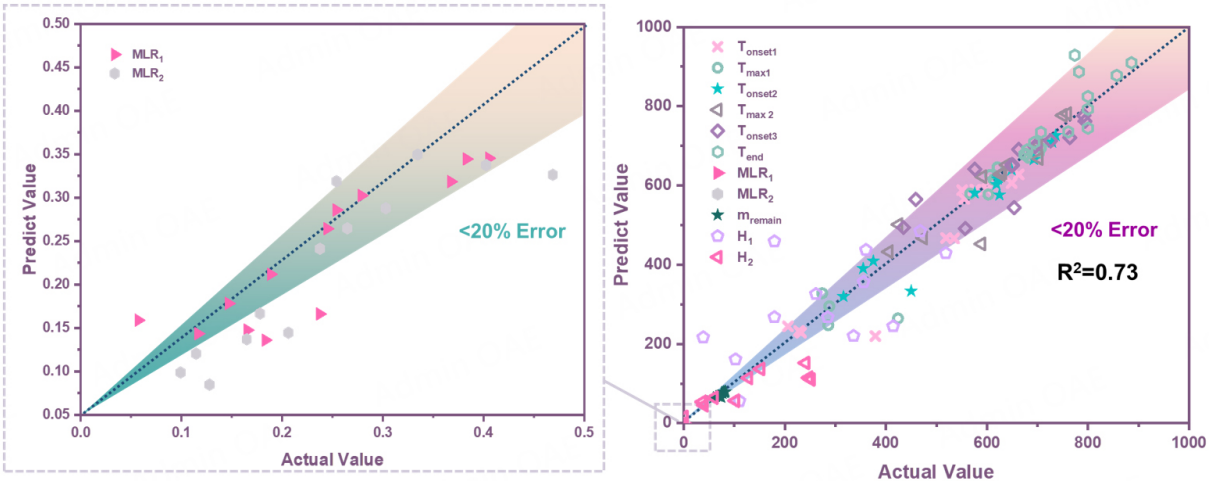

Figure 8. Predicted value *vs*. true value in the test set using the developed ANN model.

signifying that the model explains 73% of the variance in unseen data and exhibits excellent generalization ability. The R^2 values for each output parameter in the test set are provided in Supplementary Table 7. For the majority of temperature predictions, R^2 exceeds 0.8. Furthermore, the model's performance remains consistent across various data ranges, reflecting its robustness. However, some numerical predictions for H_1 show bias, likely due to significant exothermic effects from different environmental factors on the cathode with limited parameter samples.

Support vector machine (SVM) is also a robust supervised learning algorithm widely utilized in classification and regression tasks. Its fundamental principle involves identifying the optimal hyperplane in high-dimensional space to effectively separate different classes of data points. SVM demonstrates strong performance in managing high-dimensional data and exhibits notable advantages in small-sample learning and resilience to noise. Given the limited sample size of the dataset in this study and the presence of multiple output parameters, the suitability of the SVM model is evident. Therefore, this research develops the SVM model for data prediction, leveraging its strengths in complex data environments [45,46].

In this SVM model, C = 10 indicates a stronger penalty that reduces misclassification while maintaining the model's generalization ability. The parameter coef0 = 0.0 ensures that the linear and nonlinear combinations of independent variables remain unbiased in the polynomial kernel function. Additionally, gamma = 0.1 controls the influence range of the data points, with a lower gamma value effectively preventing overfitting and enhancing the model's robustness in high-dimensional space. The choice of kernel = "poly" selects a polynomial kernel, which accommodates the complex structures of nonlinear features, significantly improving classification accuracy. This well-considered combination of hyperparameters ensures the model's efficiency and precision when addressing complex data.

As illustrated in Figure 9, a comprehensive performance evaluation of the established SVM model by comparing predicted and actual values in the test set is established. The distribution of data points indicates that the prediction performance of the SVM model is average; although most points are near the diagonal, significant errors remain. R^2 for each output parameter in the test set is presented in Supplementary Table 8. The average R^2 for the training set is 0.81, signifying that the model explains approximately 81% of the variance, demonstrating a good fit. However, the average R^2 for the test set decreases to 0.64, suggesting that the model faces challenges with generalization, possibly due to overfitting. Furthermore, the average MSE for the training set is 0.015, indicating a small prediction error on the training data. In contrast, the average MSE for the test set rises to 0.033, reflecting increased prediction error on unseen data, which reinforces the conclusion regarding

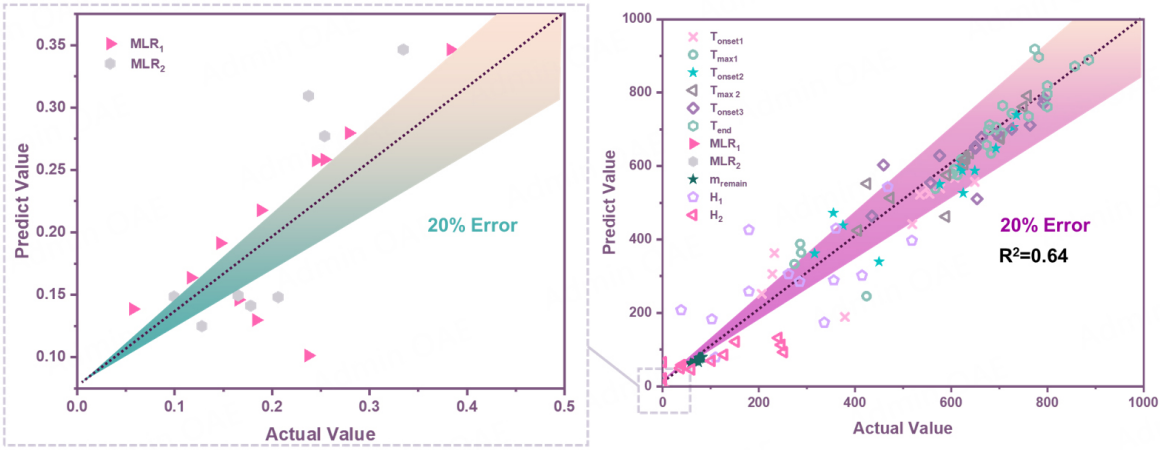

Figure 9. Predicted value *vs*. true value in the test set using the developed SVM model.

Table 8. Comparison of ANN and SVM model performance

Model	ANN		SVM	
	Parameter	**Value**	**Parameter**	**Value**
Model setting	hidden_layer_size	(16, 32, 64, 64, 32)	C	10
	activation function, solver	tanh, Sgd	coef0	0.0
	max_iter, tol	300, $1e^{-6}$	gamma	0.1
	learning_rate_init	0.01	kernel	poly
Accuracy	R^2 for training set	0.75		0.81
	R^2 for test set	0.73		0.64
	MSE for training set	0.022		0.015
	MSE for test set	0.030		0.033

the model's limited generalization ability. This issue may arise from the presence of overlapping sample inputs within the dataset[47].

Table 8 summarizes the performance of the ANN and SVM models. The R^2 of the ANN model on the test set is 0.73, significantly exceeding the SVM model's value of 0.64. This indicates that the ANN captures the intrinsic patterns in the data more effectively and demonstrates superior generalization ability. Additionally, the MSE for the ANN on the test set is 0.03, markedly lower than the SVM's MSE of 0.033, reflecting a smaller prediction error in the ANN. This superior performance can be attributed to the use of the tanh activation function in the ANN, which effectively captures nonlinear relationships and enhances the model's expressive capability. Furthermore, the deep architecture of the ANN, with layers structured as (16, 32, 64, 64, 32), enables it to learn multi-level feature representations, thereby adapting well to complex high-dimensional data. In contrast, the SVM's reliance on fixed parameter settings limits its generalization ability, particularly in small sample scenarios. Consequently, the ANN model efficiently uncovers underlying data patterns, resulting in enhanced predictive performance. This study's high-dimensional input and output parameters make ANNs ideally suited for modeling complex thermal decomposition processes, excelling at capturing intricate multi-parameter relationships. However, ANN performance is limited by dataset size; a larger dataset would yield more accurate predictions. In contrast, SVMs, while suitable for smaller datasets and simpler problems, are less effective at modeling such complex, high-dimensional interactions. The choice of ANNs represents a trade-off between their superior capabilities for handling multi-parameter systems and the need for a larger dataset.

AHP quantitative scoring framework for cathode

Researchers are required to input the elemental composition of the cathode material along with its atomic ratios and provide relevant environmental parameters. These inputs will then be processed through an ANN model

Table 9. Cathode thermal performance judgment results of NCM 811

Sample	Acronym	Experimental value	Assessed value	Total weight	Score	Total score
	T1	439	100	0.2873	28.73	
	T2	568	100	0.1427	14.27	
	T3	615	100	0.0894	8.94	
	T4	547	100	0.0503	5.03	
	T5	587	100	0.0319	3.19	
NCM811	T6	623	100	0.0216	2.16	100
	M1	0.25	100	0.074	7.4	
	M2	0.227	100	0.0408	4.08	
	M3	76.09	100	0.0225	2.25	
	H1	510.53	100	0.2053	20.53	
	H2	161.41	100	0.0342	3.42	

to attain accurate predictions. Ultimately, the analytic hierarchy process (AHP) method enables a systematic evaluation and quantitative scoring of the thermophysical parameters of cathode materials, thereby offering a robust scientific basis for assessing their safety.

In this study, all experiments were conducted using the NCM811 battery cathode material with a heating rate of 10 °C/min under an atmosphere of 5%H_2/Ar at a flow rate of 100 mL/min. By adjusting variables such as elemental atomic ratio, H2 content, gas flow rate, and heating rate, a series of experimental conditions were tested. The 11 key parameters obtained from the NCM811 material were used as a reference to evaluate the thermal decomposition risk of other materials. A higher score indicates a greater risk of thermal decomposition for the battery cathode material under the tested conditions. In this work, the evaluation result of the thermal properties of NCM811 battery cathodes under 5%H_2/Ar exposure is presented in Table 9.

T1, the initial thermal decomposition temperature of the battery cathode material, plays a critical role in influencing T2-T6. Due to its significant impact on the overall thermal decomposition process, it has been assigned the highest weight of 0.2873 in the scoring system. Additionally, the heat generated during the thermal decomposition of battery cathode materials after exposure to hydrogen and elevated temperatures is closely related to the heat release during battery thermal runaway, especially when the scale of the study is expanded. As a result, this factor is also recognized as another key parameter influencing the thermal risk of the battery material, which is assigned a weight of 0.2053. During thermal decomposition, heat is released, while heat is absorbed during the reduction phase. As a result, H1 is given a higher weight of 0.074 due to its greater role in heat generation, whereas H2 is assigned a weight of 0.048 in the thermal risk assessment.

The evaluation results of the thermal properties of cathodes with varying atomic ratios under 5%H_2/Ar exposure are presented in Supplementary Tables 9-11. These results are derived from experimental data and normalized calculations, using NCM811 (raw material) as the based parameter. The respective scores, which represent the influence of each cathode on overall thermal properties, are shown in Figure 10 as 100, 97.06, 91.71, and 86.46. The total thermal risk score for the battery cathode material, along with the scores for each primary impact factor, is clearly outlined. Specifically, among all four materials, NCM811 exhibits the highest T and H scores (64.57 and 11.48, respectively). This indicates that the NCM811 battery cathode material is more prone to thermal decomposition and releases more heat than the others, which also matches the previous analysis of the experimental data. In contrast, the M score increases with higher Co and Mn content in the cathode material. This may be attributed to the stabilizing role of Mn, which facilitates a phase transition from layered structure to spinel structure at the onset of the decomposition reaction. This transition leads to a rapid collapse of the material's crystal structure, resulting in an accelerated reaction rate. In summary, the thermal risk levels of the cathodes are ranked as follows: NCM811 > NCM622 > NCM523 > NCM111. This calculation method provides a more intuitive comparison of the thermal performances of different cathodes.

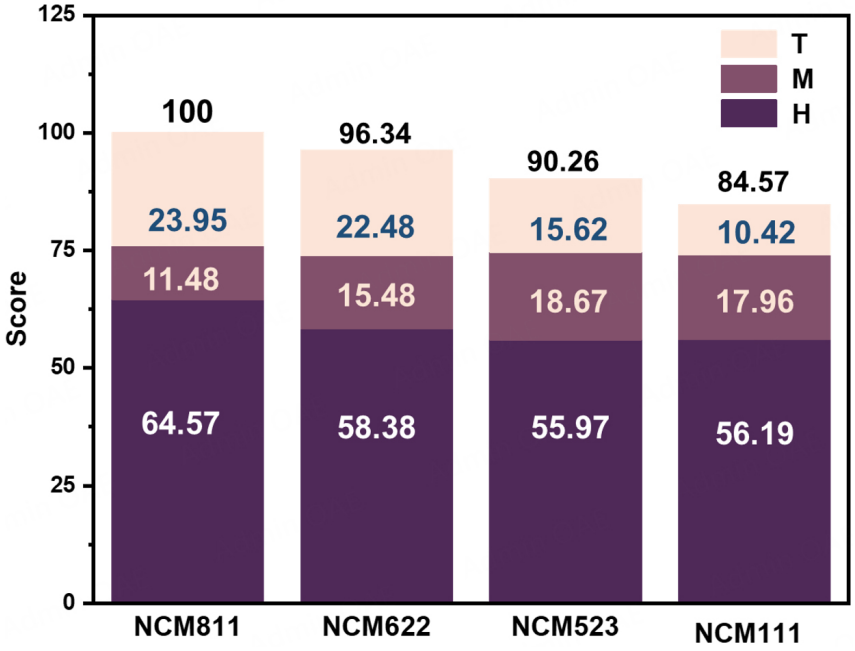

Figure 10. The result of cathode thermal risk with various elemental compositions.

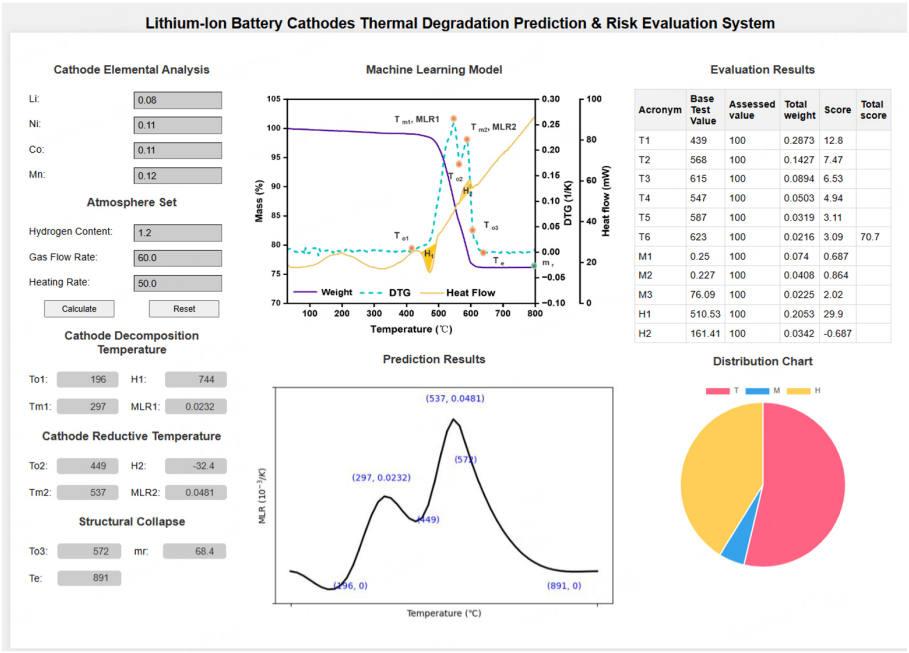

Figure 11. User interface of cathodes thermal degradation prediction & risk evaluation system (BCTR) (Available from: http://cathode.firelabxy.com/).

To enhance accessibility and usability for researchers and industry practitioners, we have developed an open-access online software platform named the Lithium-ion Battery Cathodes Thermal Degradation Prediction & Risk Evaluation System (BCTR). This tool, powered by an advanced ANN model, is designed to facilitate rapid and accurate predictions of cathode thermophysical properties and degradation behaviors under inert argon atmospheres. The software is available at http://cathode.firelabxy.com/. Figure 11 showcases the user interface of the BCTR system, where users can input the elemental composition of LIB cathodes and key

environmental parameters (e.g., hydrogen content, gas flow rate, and heating rate). Based on these inputs, the system automatically calculates critical thermophysical properties, predicts DTG curves, and provides a comprehensive risk assessment score for the thermal degradation of the selected cathode material. The BCTR system delivers results through intuitive visualizations, offering clear and actionable insights. Continuous updates will enhance the AI model by incorporating more TGA data, improving accuracy and broadening its applicability. By bridging cutting-edge machine learning with user-friendly design, BCTR represents a significant step forward in enabling the efficient evaluation of thermal safety and performance for LIB cathodes.

CONCLUSIONS

This study investigates the hydrogen attack process on ternary cathode materials and the associated factors. During the reaction, 11 key parameters were extracted: T_{o1}, T_{m1}, T_{o2}, T_{m2}, T_{o3}, T_e, MLR_1, MLR_2, H_1, H_2, and m_r. The findings indicate that, under hydrogen attack, NCM cathode materials undergo an earlier transformation from the layered structure to spinel and rock salt phases, accompanied by exothermic reactions. The atomic ratios of Li, Ni, Co and Mn have varying effects on the thermal stability of NCM. Specifically, the decomposition of NCM811 after complete delithiation occurs at 162 °C, which is 323 °C lower than the raw cathode. Additionally, higher content of H_2 accelerates the fragmentation of the cathode particles.

Pearson correlation analysis reveals the relationships among the parameters more clearly. Notably, lithium content exhibits a strong correlation (0.79) with the cathode's decomposition, while most of key temperature parameters have correlation coefficients exceeding 0.9. The correlation data establishes a solid basis for developing an ANN model for predictive analysis. After identifying the optimal hyperparameters, the model demonstrated robust predictive performance, achieving an R^2 value of 0.75 for the training set and 0.73 for the test set. Finally, thermal performance assessment (AHP) method was developed to quantitatively evaluate the thermal properties of cathode materials by weighting the key parameters.

Building on these findings, future research should focus on gathering larger, more diverse datasets to enhance model robustness and generalization. Exploring advanced machine learning algorithms, such as ensemble methods or deep learning frameworks, could further enhance predictive accuracy. Incorporating higher-dimensional parameters, including microstructural data (e.g., scanning electron microscopy images, elemental mapping, and crystallographic phase analysis), would provide deeper insights into degradation mechanisms. Additionally, integrating machine learning models with physical or thermodynamic simulations holds promise for incorporating domain-specific knowledge and refining predictions. These advancements will expand the scope of cathode material evaluation and foster innovation in next-generation battery technologies.

DECLARATIONS

Authors' contributions

Investigation, methodology, writing-original draft, formal analysis: Zhou, Y.
Investigation, Methodology: Ding, Y.
Resources, Formal analysis: Chen, Y.; Shen Y.
Methodology, Formal analysis: Wang, Z.
Experimental assistance: Li, X.
Resources, Formal analysis: Xu, J.
Conceptualization, methodology, supervision, writing-review & editing, funding acquisition: Huang, X.

Availability of data and materials

Data will be provided upon request..

Financial support and sponsorship
This work is funded by Key-Area Research and Development Program of Guangdong Province (No. 2023B0909060004).

Conflicts of interest
All authors declared that there are no conflicts of interest.

Ethical approval and consent to participate
Not applicable.

Consent for publication
Not applicable.

REFERENCES

1. Huang, W.; Feng, X.; Han, X.; Zhang, W.; Jiang, F. Questions and answers relating to lithium-ion battery safety issues. *Cell. Rep. Phys. Sci.* **2021**, *2*, 100285. DOI
2. Liu, K.; Liu, Y.; Lin, D.; Pei, A.; Cui, Y. Materials for lithium-ion battery safety. *Sci. Adv.* **2018**, *4*, eaas9820. DOI
3. Ge, S.; Leng, Y.; Liu, T.; et al. A new approach to both high safety and high performance of lithium-ion batteries. *Sci. Adv.* **2020**, *6*, eaay7633. DOI
4. Xia, Q.; Ren, Y.; Wang, Z.; et al. Safety risk assessment method for thermal abuse of lithium-ion battery pack based on multiphysics simulation and improved bisection method. *Energy* **2023**, *264*, 126228. DOI
5. Han, X.; Lu, L.; Zheng, Y.; et al. A review on the key issues of the lithium ion battery degradation among the whole life cycle. *eTransportation* **2019**, *1*, 100005. DOI
6. Liu, J.; Yadav, S.; Salman, M.; Chavan, S.; Kim, S. C. Review of thermal coupled battery models and parameter identification for lithium-ion battery heat generation in EV battery thermal management system. *Int. J. Heat. Mass. Transf.* **2024**, *218*, 124748. DOI
7. Feng, X.; Ren, D.; He, X.; Ouyang, M. Mitigating thermal runaway of lithium-ion batteries. *Joule* **2020**, *4*, 743-70. DOI
8. Shahid, S.; Agelin-Chaab, M. A review of thermal runaway prevention and mitigation strategies for lithium-ion batteries. *Energy. Convers. Man. X.* **2022**, *16*, 100310. DOI
9. Zheng, Y.; Che, Y.; Hu, X.; Sui, X.; Stroe, D.; Teodorescu, R. Thermal state monitoring of lithium-ion batteries: progress, challenges, and opportunities. *Prog. Energy. Combust. Sci.* **2024**, *100*, 101120. DOI
10. Feng, X.; Zheng, S.; Ren, D.; et al. Investigating the thermal runaway mechanisms of lithium-ion batteries based on thermal analysis database. *Appl. Energy.* **2019**, *246*, 53-64. DOI
11. Feng, X.; Ouyang, M.; Liu, X.; Lu, L.; Xia, Y.; He, X. Thermal runaway mechanism of lithium ion battery for electric vehicles: a review. *Energy. Storage. Mater.* **2018**, *10*, 246-67. DOI
12. Gustafsson, O.; Kullgren, J.; Brant, W. R. Low-temperature cation ordering in high voltage spinel cathode material. *ACS. Appl. Energy. Mater.* **2023**, *6*, 5000-8. DOI
13. Duan, Y.; Chen, S.; Zhang, L.; Guo, L.; Shi, F. Review on oxygen release mechanism and modification strategy of nickel-rich NCM cathode materials for lithium-ion batteries: recent advances and future directions. *Energy. Fuels.* **2024**, *38*, 5607-31. DOI
14. Li, Y.; Liu, X.; Wang, L.; et al. Thermal runaway mechanism of lithium-ion battery with $LiNi_{0.8}Mn_{0.1}Co_{0.1}O_2$ cathode materials. *Nano. Energy.* **2021**, *85*, 105878. DOI
15. Shadike, Z.; Lee, H.; Borodin, O.; et al. Identification of LiH and nanocrystalline LiF in the solid-electrolyte interphase of lithium metal anodes. *Nat. Nanotechnol.* **2021**, *16*, 549-54. DOI
16. Nam, K.; Bak, S.; Hu, E.; et al. Combining in situ synchrotron X-ray diffraction and absorption techniques with transmission electron microscopy to study the origin of thermal instability in overcharged cathode materials for lithium-ion batteries. *Adv. Funct. Mater.* **2013**, *23*, 1047-63. DOI
17. Liu, X.; Ren, D.; Hsu, H.; et al. Thermal runaway of lithium-ion batteries without internal short circuit. *Joule* **2018**, *2*, 2047-64. DOI
18. Wang, Y.; Ren, D.; Feng, X.; Wang, L.; Ouyang, M. Thermal runaway modeling of large format high-nickel/silicon-graphite lithium-ion batteries based on reaction sequence and kinetics. *Appl. Energy.* **2022**, *306*, 117943. DOI
19. Wu, Y.; Feng, X.; Liu, X.; et al. In-built ultraconformal interphases enable high-safety practical lithium batteries. *Energy. Storage. Mater.* **2021**, *43*, 248-57. DOI
20. Qiu, B.; Zhang, M.; Wu, L.; et al. Gas-solid interfacial modification of oxygen activity in layered oxide cathodes for lithium-ion batteries. *Nat. Commun.* **2016**, *7*, 12108. DOI
21. Wang, Y.; Feng, X.; Peng, Y.; et al. Reductive gas manipulation at early self-heating stage enables controllable battery thermal failure.

Joule **2022**, *6*, 2810-20. DOI
22. Qamar, R.; Ali, Zardari, B. Artificial neural networks: an overview. *Mesopotamian. J. Comput. Sci.* **1993**, *30*. DOI
23. Chen, J.; Qi, G.; Wang, K. Synergizing machine learning and the aviation sector in lithium-ion battery applications: a review. *Energies* **2023**, *16*, 6318. DOI
24. Liang, L.; Li, X.; Zhao, F.; et al. Construction and operating mechanism of high-rate Mo-doped $Na_3V_2(PO_4)_3$@C nanowires toward practicable wide-temperature-tolerance Na-ion and hybrid Li/Na-ion batteries. *Adv. Energy. Mater.* **2021**, *11*, 2100287. DOI
25. Liu, Z.; Yang, X. Thermal stability enhancement and prediction by ANN model. *Energy. AI.* **2024**, *16*, 100348. DOI
26. Burgaz, E.; Yazici, M.; Kapusuz, M.; Alisir, SH.; Ozcan, H. Prediction of thermal stability, crystallinity and thermomechanical properties of poly(ethylene oxide)/clay nanocomposites with artificial neural networks. *Thermochim. Acta.* **2014**, *575*, 159-66. DOI
27. Kurucan M.; Özbaltan M.; Yetgin Z.; Alkaya A. Applications of artificial neural network based battery management systems: a literature review. *Renew. Sustain. Energy. Rev.* **2024**, *192*, 114262. DOI
28. Ng, M.; Sun, Y.; Seh, ZW. Machine learning-inspired battery material innovation. *Energy. Adv.* **2023**, *2*, 449-64. DOI
29. Chen Y.; Wang Z.; Lin S.; Qin Y.; Huang X. A review on biomass thermal-oxidative decomposition data and machine learning prediction of thermal analysis. *Clean. Mater.* **2023**, *9*, 100206. DOI
30. Ren, D.; Liu, X.; Feng, X.; et al. Model-based thermal runaway prediction of lithium-ion batteries from kinetics analysis of cell components. *Appl. Energy.* **2018**, *228*, 633-44. DOI
31. Ren, D.; Feng, X.; Liu, L.; et al. Investigating the relationship between internal short circuit and thermal runaway of lithium-ion batteries under thermal abuse condition. *Energy. Storage. Mater.* **2021**, *34*, 563-73. DOI
32. Manthiram, A.; Song, B.; Li, W. A perspective on nickel-rich layered oxide cathodes for lithium-ion batteries. *Energy. Storage. Mater.* **2017**, *6*, 125-39. DOI
33. Manthiram, A.; Vadivel, Murugan, A.; Sarkar, A.; Muraliganth, T. Nanostructured electrode materials for electrochemical energy storage and conversion. *Energy. Environ. Sci.* **2008**, *1*, 621. DOI
34. Huang, Z.; Yu, D.; Makuza, B.; Tian, Q.; Guo, X.; Zhang, K. Hydrogen reduction of spent lithium-ion battery cathode material for metal recovery: mechanism and kinetics. *Front. Chem.* **2022**, *10*, 1019493. DOI
35. Zhang, Y.; Wang, H.; Li, W.; Li, C.; Ouyang, M. Size distribution and elemental composition of vent particles from abused prismatic Ni-rich automotive lithium-ion batteries. *J. Energy. Storage.* **2019**, *26*, 100991. DOI
36. Wu, C.; Wu, Y.; Feng, X.; et al. Ultra-high temperature reaction mechanism of $LiNi_{0.8}Co_{0.1}Mn_{0.1}O_2$ electrode. *J. Energy. Storage.* **2022**, *52*, 104870. DOI
37. Zheng, J.; Liu, T.; Hu, Z.; et al. Tuning of thermal stability in layered $Li(Ni_xMn_yCo_z)O_2$. *J. Am. Chem. Soc.* **2016**, *138*, 13326-34. DOI
38. Bak, S.; Nam, K.; Chang, W.; et al. Correlating structural changes and gas evolution during the thermal decomposition of charged $Li_xNi_{0.8}Co_{0.15}Al_{0.05}O_2$ cathode materials. *Chem. Mater.* **2013**, *25*, 337-51. DOI
39. Li, K.; Huang, X.; Fleischmann, C.; Rein, G.; Ji, J. Pyrolysis of medium-density fiberboard: optimized search for kinetics scheme and parameters via a genetic algorithm driven by kissinger's method. *Energy. Fuels.* **2014**, *28*, 6130-9. DOI
40. Lee, SH.; Moon, J.; Lee, M.; Yu, T.; Kim, H.; Park, B. M. Enhancing phase stability and kinetics of lithium-rich layered oxide for an ultra-high performing cathode in Li-ion batteries. *J. Power. Sources.* **2015**, *281*, 77-84. DOI
41. Hatsukade T.; Schiele A.; Hartmann P.; Brezesinski T.; Janek J. Origin of carbon dioxide evolved during cycling of nickel-rich layered NCM cathodes. *ACS. Appl. Mater. Interfaces.* **2018**, *10*, 38892-9. DOI
42. Li, M.; Lu, J.; Chen, Z.; Amine, K. 30 Years of lithium-ion batteries. *Adv. Mater.* **2018**, *30*, e1800561. DOI
43. Bonnick, P.; Muldoon, J. The quest for the holy grail of solid-state lithium batteries. *Energy. Environ. Sci.* **2022**, *15*, 1840-60. DOI
44. Choi, J. Investigation of the correlation of building energy use intensity estimated by six building performance simulation tools. *Energy. Build.* **2017**, *147*, 14-26. DOI
45. Anifowose, F.; Labadin, J.; Abdulraheem, A. Improving the prediction of petroleum reservoir characterization with a stacked generalization ensemble model of support vector machines. *Appl. Soft. Comput.* **2015**, *26*, 483-96. DOI
46. Cortes, C.; Vapnik, V. Support-vector networks. *Mach. Learn.* **1995**, *20*, 273-97. DOI
47. Otchere, D. A.; Arbi Ganat, T. O.; Gholami, R.; Ridha, S. Application of supervised machine learning paradigms in the prediction of petroleum reservoir properties: comparative analysis of ANN and SVM models. *J. Pet. Sci. Eng.* **2021**, *200*, 108182. DOI